Spatially Variable Advection Correction of Radar Data. Part II: Test Results

ALAN SHAPIRO

*School of Meteorology, and Center for Analysis and Prediction of Storms, University of Oklahoma,
Norman, Oklahoma*

KATHERINE M. WILLINGHAM

*Cooperative Institute for Mesoscale Meteorological Studies, University of Oklahoma, and NOAA/OAR/National
Severe Storms Laboratory, Norman, Oklahoma*

COREY K. POTVIN

*School of Meteorology, and Center for Analysis and Prediction of Storms, and Cooperative Institute
for Mesoscale Meteorological Studies, University of Oklahoma, Norman, Oklahoma*

(Manuscript received 9 February 2010, in final form 27 May 2010)

ABSTRACT

The spatially variable advection-correction/analysis procedure introduced in Part I is tested using analytical reflectivity blobs embedded in a solid-body vortex, and Terminal Doppler Weather Radar (TDWR) and Weather Surveillance Radar-1988 Doppler (WSR-88D) data of a tornadic supercell thunderstorm that passed over central Oklahoma on 8 May 2003. In the TDWR tests, plan position indicator (PPI) data at two volume scan times are input to the advection-correction procedure, with PPI data from a third scan time, intermediate between the two input times, that is used to validate the results. The procedure yields analyzed reflectivity fields with lower root-mean-square errors and higher correlation coefficients than those reflectivity fields that were advection corrected with any constant advection speed.

1. Introduction

Attempts to mitigate errors in data analysis arising from the nonsimultaneity of the data collection have numerous applications in radar, mesoscale, and satellite meteorology and in hydrology. Research on this problem has largely focused on the advection problem and the development of advection-correction/analysis procedures in which the horizontal advection components of patterns (e.g., of radar reflectivity) are estimated and then used to shift the nonsimultaneously gathered data to analysis grid points at a common analysis time. In most of these procedures, the advection components are treated as constant. In Part I of this study (Shapiro et al. 2010, hereafter Part I) we reviewed the use of these techniques in radar meteorology and introduced a Lagrangian procedure for the advection-correction/analysis of reflectivity

data in which the advection components varied spatially. In the proposed method, the reflectivity-pattern trajectories, horizontal advection fields, and reflectivity fields are to be analyzed simultaneously using a combined analytical and numerical solution of the Euler–Lagrange equations. The cost function underpinning the procedure is very similar to those of some single-Doppler velocity retrievals, especially the variational echo tracking (VET) procedure (Laroche and Zawadzki 1995), but the intended application is advection correction of radar data rather than retrieval of air velocity. In this companion paper (Part II), the procedure is tested using analytical and real data.

In section 2 we consider the advection of analytical reflectivity blobs embedded in a solid-body vortex. Although the input reflectivity field satisfies the frozen-turbulence constraint exactly, the velocity components in a solid-body vortex do not satisfy the natural boundary conditions for the analysis procedure (which were shown in Part I to be zero-normal-gradient conditions) and do not yield minimum values for the smoothness constraints (only constant values would minimize those

Corresponding author address: Alan Shapiro, School of Meteorology, University of Oklahoma, 120 David L. Boren Blvd., Room 5900, Norman, OK 73072.
E-mail: ashapiro@ou.edu

terms). Accordingly, although these tests are highly idealized, they are not true identical twin tests, and possible weaknesses of the analysis procedure stemming from the natural boundary conditions and smoothness constraints can be examined.

In section 3 the procedure is tested using terminal Doppler weather radar (TDWR) and Weather Surveillance Radar-1988 Doppler (WSR-88D) data of a tornadic supercell thunderstorm that passed over the southern Oklahoma City metropolitan area on 8 May 2003. Throughout much of its mature phase, the storm was relatively close to three Doppler radars: KTLX (WSR-88D radar in southeastern Oklahoma City), KOUN (dual-polarized prototype WSR-88D radar in central Norman), and KOKC (TDWR radar in northwestern Norman). Data from this well-sampled storm have been used in dynamical and microphysical analyses (Romine et al. 2008; Kumjian and Ryzhkov 2008, 2009), storm-scale data assimilation (Hu and Xue 2007; Dowell and Wicker 2009; Aksoy et al. 2009), and evaluations of tornado-detection procedures (Ryzhkov et al. 2005; Liu et al. 2007; Wang et al. 2008; Potvin et al. 2009). The storm's close proximity to the radars and its fast (and spatially variable) advection speed (~ 17 m s^{-1} toward the east-northeast) make it a good test case. These real-data tests allow us to examine the procedure in a much less idealized setting than the solid-body vortex test; in the real-data case all of the constraints and boundary conditions are presumably inappropriate to some degree.

2. Solid-body vortex tests

In preliminary tests (not shown) of the spatially variable analysis procedure with a solid-body vortex test case and 8 May 2003 data from a WSR-88D radar (KTLX, which has 1-km radial resolution for the reflectivity field), the procedure would fail to converge, converge to physically unreasonable solutions, or exhibit strong sensitivity to the trajectory time step if the analysis grid spacing was much smaller than the spatial resolution of the data and the trajectory time step was very small. These problems stemmed from large (and spurious) gradients of input reflectivity data resolved on the analysis grid when spatially coarse data were represented with very high spatial resolution. The problems disappeared when the spatial resolution for the analysis grid was made comparable to that of the data. Preliminary tests also showed that a slight smoothing of the input reflectivity data benefited the analysis. In the solid-body vortex experiments of this section, and the 8 May 2003 experiments of section 3, the input data were subjected to a nine-point smoother, a three-point smoother applied successively in the x and y directions following (11–87) of Haltiner and Williams

(1980). Such a smoother removes small-scale grid noise (two-gridlength waves) in the data; although it also dampens other wavelengths, its effect decreases rapidly with wavelength.

In the solid-body vortex tests, the "true" reflectivity field consisted of reflectivity blobs advected by an axisymmetric vortex of constant angular velocity. The vortex was centered on the lower left corner ($x = 0$, $y = 0$) of a square analysis domain. The reflectivity data were specified as a superposition of a spatially periodic array of blobs rotating with the vortex, and a stationary pattern of grid-scale noise,

$$R = c \sin^2\left[b\left(\frac{r-a}{a}\right)\right]\sin^2[4(\theta - \omega t)] + R_{\mathrm{noise}} \quad \text{and} \tag{2.1}$$

$$R_{\mathrm{noise}} = d \sin\left(\frac{2\pi x}{\lambda_{\mathrm{noise}}}\right)\sin\left(\frac{2\pi y}{\lambda_{\mathrm{noise}}}\right), \tag{2.2}$$

where R is the true reflectivity field, R_{noise} is the reflectivity field associated with the noise, ω is the vortex angular velocity, and $r = \sqrt{x^2 + y^2}$ and $\theta = \sin^{-1}(y/r)$ are, respectively, the radial and azimuthal coordinates of an analysis point in a cylindrical coordinate system centered on the vortex. Since the analysis domain is in the first quadrant ($x \geq 0$, $y \geq 0$), the principal branch of the inverse sine should be considered in the evaluation of θ.

The test parameters were specified as $a = 25$ km, $b = 5$ (dimensionless), $c = 50$ dBZ, $d = 5$ dBZ (so amplitude d of the noise was 10% of the amplitude c of the blobs), $\omega = 0.0004$ s^{-1}, and $\lambda_{\mathrm{noise}} = \Delta x/7.3$. This latter value was chosen so that the waves comprising R_{noise} would be too small to be resolved on the analysis grid, and the phases of these waves at adjacent grid points would not be equal. The analysis grid was a 50 km $\times$ 50 km square with a grid spacing of $\Delta x = \Delta y = 500$ m. The scan period was $T = 300$ s, and the time step for the trajectory calculation was $\Delta t = 15$ s. The convergence thresholds for the relaxation algorithm and the overall procedure were set at 10^{-3} and 10^{-1} m s^{-1}, respectively. The procedure was initialized with U and V set to zero. Experiments focused on the sensitivity of the analyzed fields to the smoothness weight β, introduced in Part I [see (2.1) and the subsequent description]. Tests were performed with $\beta = 1, 3, 10, 100$, and 200 dBZ^2.

The reflectivity data were obtained by evaluating (2.1) and (2.2) on the analysis grid at the two constant altitude plan position indicator (CAPPI) times $t = 0$ and $t = T$ and then applying the nine-point smoother. These input fields along with the analyzed reflectivity field at an intermediate time ($t = T/2$) from the experiment with $\beta = 100$ dBZ^2 are shown in Fig. 1. Despite application of the
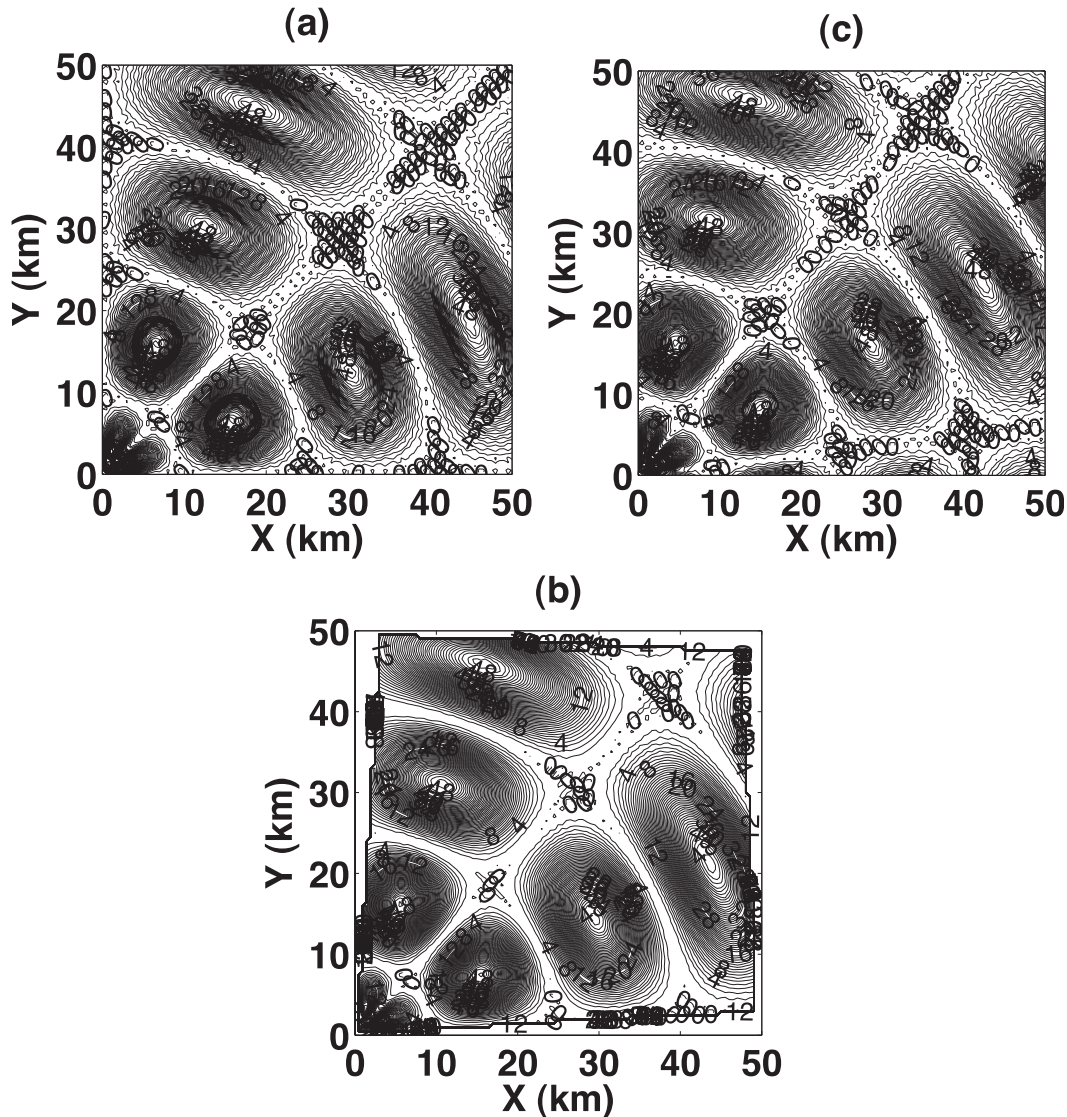
FIG. 1. Advection of reflectivity blobs in a solid-body vortex. The input data are obtained from (2.1) and (2.2) at (a) $t = 0$ and (c) $t = 360$ s. (b) The advection-corrected reflectivity for the $\beta = 100$ dBZ^2 experiment at the intermediate time $t = 180$ s. Contour interval is 4 dBZ.

smoother, the reflectivity field at the two input times still has a noisy (corrugated) appearance.

The spatially variable advection components we seek to recover are the Cartesian wind components associated with a solid-body vortex:

$$U = -\omega y \quad \text{and} \quad V = \omega x. \quad (2.3)$$

For the domain size and vortex intensity considered in these tests, (2.3) yields peak magnitudes of U and V of 20 m s^{-1}. These peaks should be attained along the northern edge of the domain for U and along the eastern edge for V. However, (2.3) shows that the zero-normal-gradient boundary conditions imposed in the analysis

are not consistent with the solid-body vortex U on north–south boundaries or V on east–west boundaries. As we will see, the largest errors in our analyzed U field are associated with these southern and northern boundaries. Since the V field is essentially the same as the U field rotated by 90°, results will only be shown for the U field.

As shown in Fig. 2, experiments with β in a 3–100-dBZ^2 range yielded advection fields that were relatively insensitive to β, although with the expected tendency for larger values of β to be associated with smoother advection fields. Figure 2 shows that the analyses captured the main trend in the spatial dependence of the U field. The greatest errors in U were evident on the north and
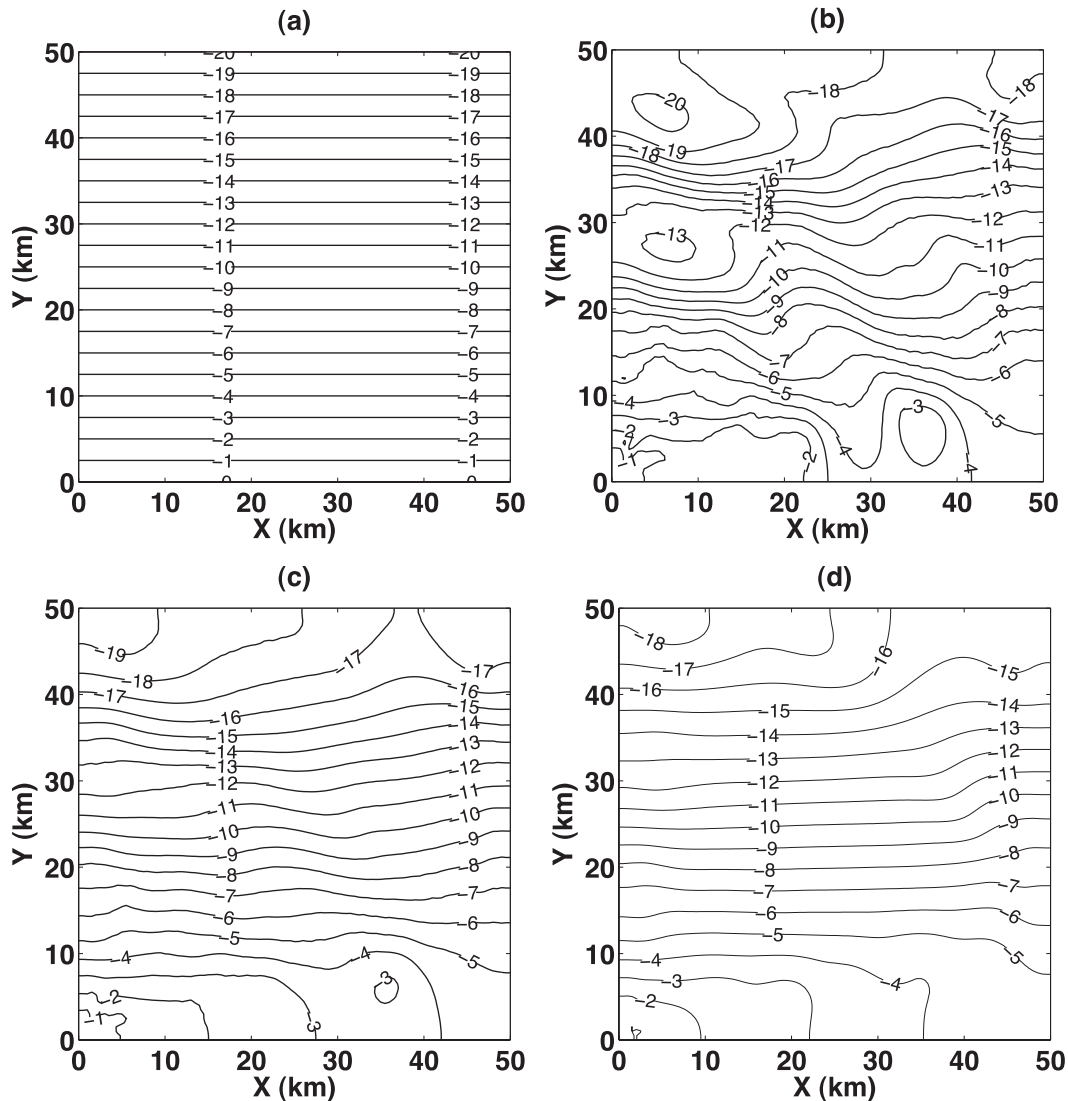
FIG. 2. Contour plot of U field in a solid-body vortex (a) from the exact solution (2.3), and (b)–(d) from the spatially variable advection correction experiments with (b) $\beta = 3$ dBZ^2, (c) $\beta = 10$ dBZ^2, and (d) $\beta = 100$ dBZ^2. Contour interval is 1 m s^{-1}.

south boundaries, where the zero-normal-gradient condition forced isolines of U to approach the boundaries at right angles, in contrast to the behavior of the true U field. The experiment with $\beta = 200$ dBZ^2 (not shown) yielded a U field very similar to that obtained with $\beta = 100$ dBZ^2. The experiment with $\beta = 1$ dBZ^2 (not shown) yielded a noisy and distorted U field and did not fully converge.

For the experiments shown in Fig. 2, the analyzed reflectivity field at the time midway between the two CAPPI times ($t = T/2 = 180$ s) was examined and found to be in qualitatively good agreement with the true reflectivity field (individual blobs at the middle time were approximately halfway between their respective locations at the first and second CAPPI times). An example

of the advection-corrected reflectivity field at this middle time is shown in Fig. 1b. Figure 1 also shows that the advection-corrected reflectivity field is less noisy than the two input reflectivity fields, illustrating the smoothing effect of combining data from the two end points of the trajectories. Figure 1 also shows that the footprint of analyzed data is slightly less than the area of the analysis domain. The data voids near the edges of the analysis domain arise from missing data at one or both end points of the trajectories.

The root-mean-square error (RMSE) in the retrieved reflectivity field at $t = T/2$ for the experiment shown in Fig. 2 was 0.83 dBZ. For an experiment in which the azimuthal wavenumber in the true reflectivity field was

reduced by a factor of 2 from the default value [the number multiplying θ in (2.1) reduced from 4 to 2], the RMSE dropped to 0.46 dBZ. In experiments in which the azimuthal wavenumber was doubled and tripled from its default value, the RMSE increased to 1.30 and 1.66 dBZ, respectively. However, a further decrease in the scale of the disturbance (azimuthal wavenumber quadrupled from the default value) yielded an RMSE of 20.99 dBZ. Such a catastrophic result was associated with reflectivity blobs that were too small to be properly resolved on the analysis grid—in some regions the true reflectivity changed by an amount equal to the peak amplitude 50 dBZ over a distance of less than one analysis grid interval.

3. TDWR and WSR-88D test case: 8 May 2003 supercell thunderstorm

In this section we report on experiments using KOKC (a TDWR radar) and KTLX (a WSR-88D radar) data of a tornadic supercell thunderstorm that passed over central Oklahoma on 8 May 2003. Since operational TDWRs scan their lowest elevation angle much more frequently (up to ~1-min return time) than operational WSR-88Ds (~4–5-min return time), it is convenient to focus the quantitative verification on experiments using data from these lowest-level TDWR scans: scans are thinned in time to yield a temporal resolution comparable to that of WSR-88D data, and the subsequent analysis is compared to an intermediate (withheld) TDWR scan. We used WSR-88D data only in qualitative tests.

Deployed near major U.S. airports, TDWRs are C-band Doppler radars designed to detect microbursts, wind shear, and other aviation hazards (Michelson et al. 1990; Vasiloff 2001; Shun et al. 2003; NOAA/NWS 2005). The radial velocity and reflectivity fields are sampled with a range resolution of 150 m. The half-power beamwidth is 0.55°, but because of processing and communications limitations in the radar data acquisition computer, the data are degraded to an azimuthal resolution of $\Delta\phi = 1.0°$. The TDWR reflectivity data are known to suffer from attenuation in heavy precipitation, but the Doppler velocities are relatively unaffected as long as there is sufficient return power to the radar. In contrast, the WSR-88D S-band Doppler radars have a range resolution of 1 km (for reflectivity) and a half-power beamwidth of 0.95° and suffer relatively little attenuation (Crum and Alberty 1993; Klazura and Imy 1993). Since the 8 May 2003 supercell storm was in its most intense phase when it was passing through the southern Oklahoma City metropolitan area north of the KOKC radar, one would expect significant attenuation of the KOKC reflectivity on the northern side of the storm during that period. A

visual comparison of the reflectivity imagery from the KOKC (Fig. 8a) and KTLX (Fig. 13) radars over the same analysis domain strongly suggests this was indeed the case (note especially the reflectivity differences in the region 20 km $< x <$ 30 km, $y >$ 15 km).

Tests were performed using data from the lowest KOKC elevation angle (0.6° scans) at 2222:55, 2225:16, and 2227:17 UTC. Data from the first and third scans were supplied to the advection-correction procedure [so the two plan position indicator (PPI) times were spaced slightly more than 4 min apart], while data from the second (middle) scan were used to validate the results. Data from these three scans were manually edited using SOLO II software (Oye et al. 1995) and then interpolated to a 60 km × 35 km (x, y) Cartesian analysis grid with a grid spacing of $\Delta x = \Delta y = 500$ m using REORDER software (Oye and Case 1995). This latter step used two-dimensional Cressman interpolation (Haltiner and Williams 1980) with a radius of influence that expanded with range ($R_c = 0.9°r$) to account for the spread of the data at larger radar probe volumes. The analysis grid enclosed most of the storm, including the attenuated northern region, at all three observation times. Details of the editing, quality-controlling, and interpolation procedures are described in Donner (2007). Figure 3 depicts PPIs of the KOKC reflectivity and radial velocity fields from the two input times, 2222:55 and 2227:17 UTC.

The spatially variable analysis procedure was run with a computational time step of $\Delta t = 17.47$ s, a value chosen to yield parcel displacements of less than one grid interval over one time step, while also insuring that one of the computational times would be very close to the middle (verification) PPI time. The convergence thresholds for the relaxation algorithm and the overall procedure were set at 10^{-3} and 10^{-2} m s^{-1}, respectively. The results were quantitatively verified by comparing the KOKC reflectivity PPI constructed at 2225:16 UTC with the interpolation procedure described above to the advection-corrected reflectivity at the computational time closest to this PPI time. The chosen computational time was within 2 s of that PPI time. For each experiment we calculated the RMSE and correlation coefficient (Cor),

$$\text{RMSE} = \sqrt{\frac{1}{n}\sum(X - Y)^2} \quad \text{and}$$

$$\text{Cor} = \frac{\sum XY - \left(\sum X\right)\left(\sum Y\right)\Big/ n}{\sqrt{\sum X^2 - \left(\sum X\right)^2 \Big/ n}\sqrt{\sum Y^2 - \left(\sum Y\right)^2 \Big/ n}},$$
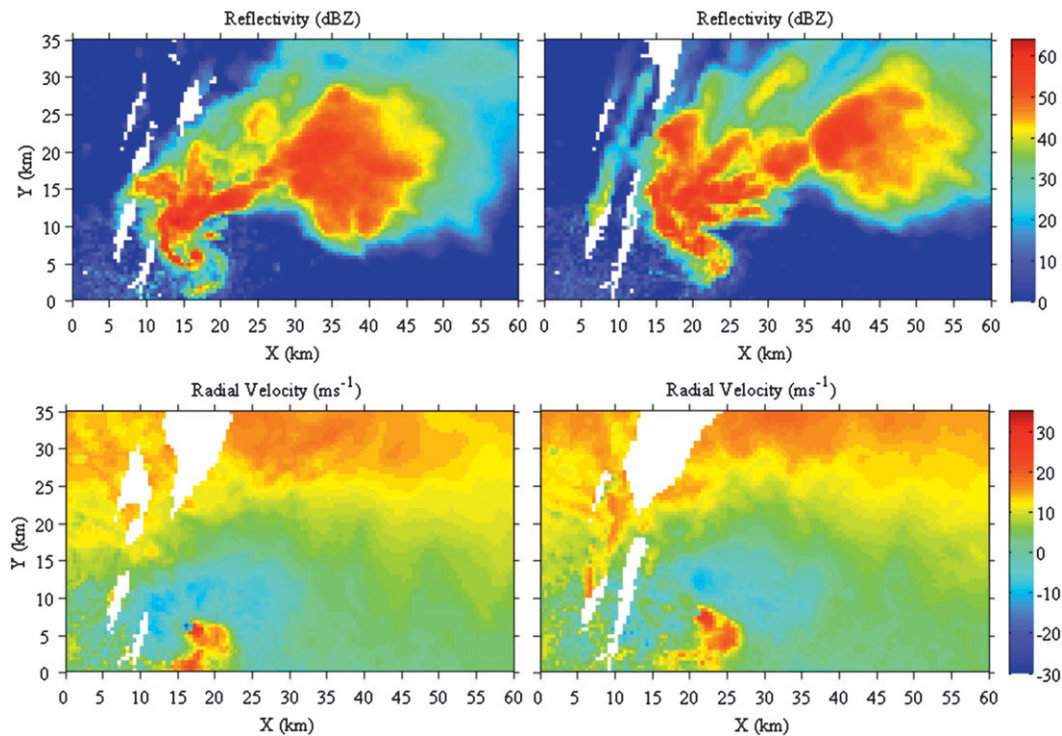
$$(3.1)$$

FIG. 3. (top) Reflectivity and (bottom) radial velocity from the 0.6° elevation angle of the KOKC radar on 8 May 2003 at (left) 2222:55 and (right) 2227:17 UTC. Data are displayed on the Cartesian analysis grid used in the advection-correction experiments. White areas indicate missing values. The radar is approximately 7.43 km south and 7.31 km east of the origin (0, 0) of the analysis grid.

where X is an advection-corrected variable, Y the corresponding observed variable, and the sums extend over the n analysis grid points for which both advection-corrected and observed variables are available.

To help gauge the merit of the spatially variable advection-correction procedure, the statistical results were compared with those from three sets of constant U, V advection-correction experiments in which U and V were each set to a succession of values ranging from 0 to 25 m s^{-1} in 1 m s^{-1} increments (26^2 experiments in each set). The same trajectory/interpolation subroutines and parameter settings used in the spatially variable procedure were used in these constant U, V experiments. A first set of constant U, V experiments was performed with forward-only trajectory analyses, that is, with parcels advected forward in time to the second PPI time (2227:17 UTC) and no use made of data from the first PPI time (2222:55 UTC). The resulting statistics are presented in Fig. 4. A corresponding set of constant U, V experiments was performed with backward-only trajectory analyses (Fig. 5) and with combined (via linear interpolation on each trajectory) forward and backward trajectory analyses (Fig. 6). In all three sets of experiments, the best results (in terms of lowest RMSE and highest correlation coefficient) were obtained for a similar

pair of U, V values ($U = 15$ m s^{-1}, $V = 10$ m s^{-1}). These values are consistent with what one could estimate visually from the en masse advection of the storm in the reflectivity imagery of Fig. 3. The results from the combined forward and backward trajectory experiments (Fig. 6) were notably better than those from either the forward-only (Fig. 4) or backward-only (Fig. 5) trajectory experiments. This suggested that the evolution effects apparent in several regions of the storm in the reflectivity imagery (e.g., regions of new convection in the hook echo and just north and south of the hook echo) were better accounted for when information at both input times were combined.

Spatially variable advection-correction experiments were performed with a range of smoothness weights. The procedure was initialized with first guesses of $U \simeq 4.5$ m s^{-1} and $V \simeq 3.4$ m s^{-1} that were obtained from a single pass of the Gal-Chen (1982) reflectivity-based procedure (i.e., a noniterative version). As seen in Fig. 6, these first-guess values are not very close to the optimal constant values, although they are at least in the same quadrant as those values. Experiments with β ranging from 75 to 1000 dBZ^2 converged in 20–40 s of CPU time on a two-processor Mac Pro (2.66-GHz dual-core Intel Xeon) running Intel FORTRAN 9.1 with OS 10.4.11.
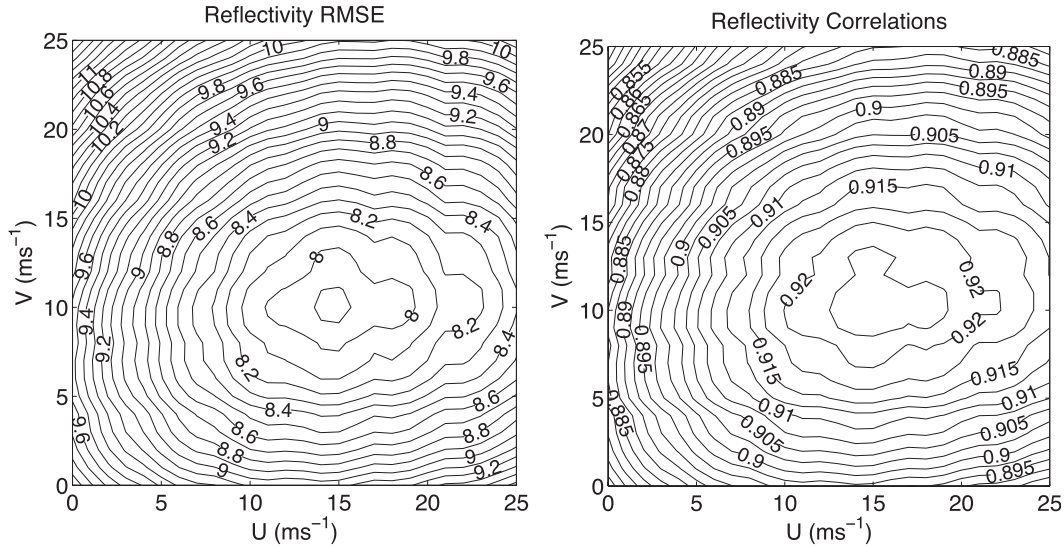
FIG. 4. Contour plots of reflectivity (left) RMSE and (right) Cor for 8 May 2003 KOKC advection-correction experiments with imposed constant U, V components and forward-only trajectory analyses. Results are valid at 2225:16 UTC. Contour interval for reflectivity RMSE is 0.1 dBZ. Contour interval for reflectivity Cor is 0.0025.

Experiments with $\beta = 25$ dBZ^2 and $\beta = 50$ dBZ^2 were also run, although the algorithm had not converged by the end of those runs (i.e., after 100 iterations). As seen in Table 1, the RMSE and Cor values for all of these spatially variable experiments, even those that had not yet converged, were better than those for any of the constant U, V experiments (Figs. 4–6). The RMSEs in most of the spatially variable experiments were about 15% lower than the lowest RMSE ($\simeq$5.3 dBZ) in the best constant U, V experiment. The results from the spatially variable experiments are quite similar for a broad

range of these β, although the results for $\beta = 1000$ dBZ^2 and larger (not shown) begin to degrade, as do the results for $\beta = 75$ dBZ^2 and smaller.

Inspection of the analyzed U and V fields (not shown) reveals that the $\beta = 25$ dBZ^2 and $\beta = 50$ dBZ^2 results are fairly noisy. That the reflectivity analyses for those cases are still better than those for any constant U, V experiment is likely due to the fact that U and V appear in integrated form in the reflectivity analysis (3.10) and (3.11) of Part I, and integration is a smoothing (noise reducing) process. In the experiments with β ranging
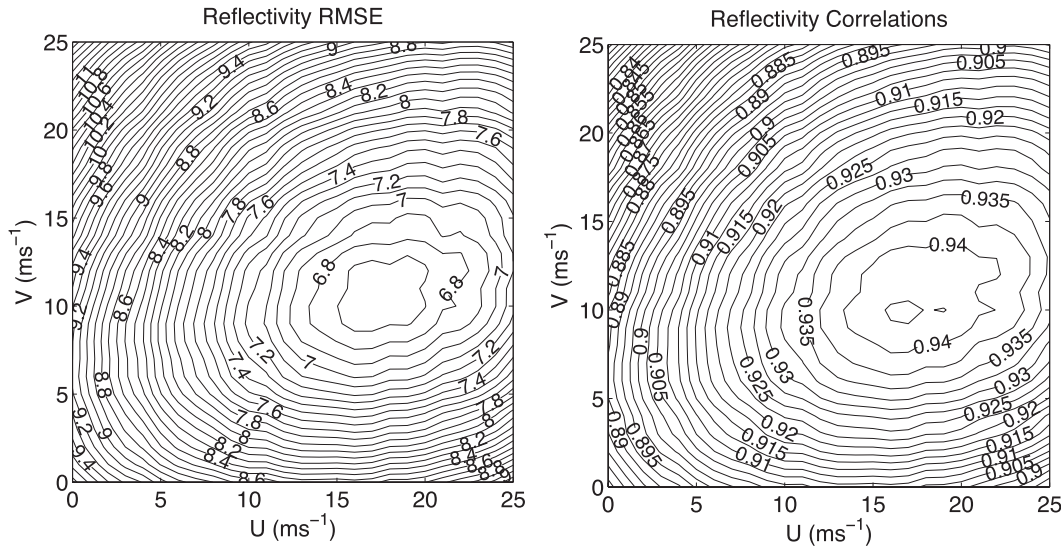

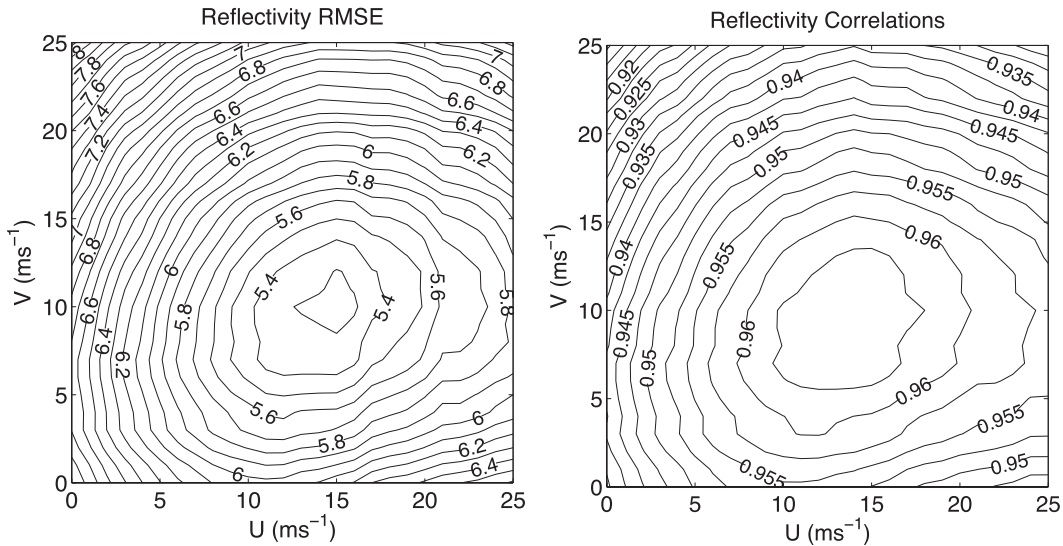FIG. 5. As in Fig. 4, but for backward-only trajectory analyses.

FIG. 6. As in Fig. 4, but for combined forward and backward trajectory analyses.

from 100 to 1000 dBZ^2 there is relatively little change in U or V other than a slight progressive smoothing with increasing β. This behavior is consistent with that seen in the solid-body vortex tests of section 2. As a representative example, we consider the U, V fields from the $\beta = 400$ dBZ^2 experiment (Fig. 7). The most salient feature is the eastward intensification of the westerly advection component (U). This intensification is consistent with what can be inferred visually from the reflectivity field at the two time levels in Fig. 3: the far western edge of the storm and the hook echo on the southwestern part of the storm both advect eastward more slowly than the forward flank (northeastern part of storm). The V field is more complex, and although the magnitudes of V are generally less than that of U, comparison with Fig. 3 shows that the V field asymmetries provide a reasonable

account of the north–south motions of the reflectivity pattern. We note that the zone of very small ($\simeq 0$ m s^{-1}) values of V in the north-central part of the domain is likely a consequence of attenuation.

TABLE 1. RMSE and Cor for spatially variable advection-correction experiments using 8 May 2003 KOKC radar data. Data for R and v_r from the 0.6° KOKC PPI scans at 2222:55 and 2227:17 UTC are input to the procedure. Advection-corrected fields are output at a time corresponding to a third (intermediate) PPI scan, 2225:16 UTC, and compared to the data at that time. Experiments B25–B1000 are spatially variable advection-correction experiments with smoothness weights β ranging from 25 dBZ^2 (experiment B25) to 1000 dBZ^2 (experiment B1000). An asterisk indicates that the procedure had not yet converged.

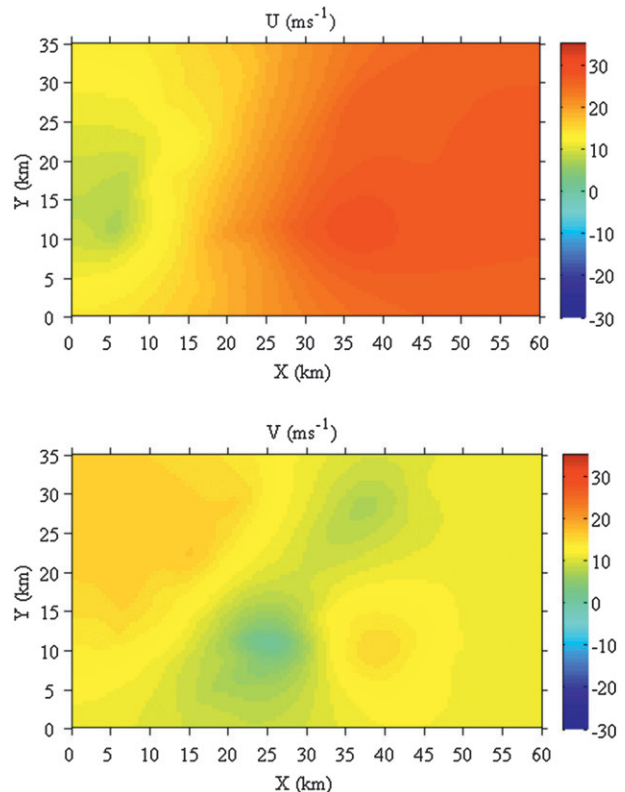|	B25*	B50*	B75	B100	B200	B400	B600	B1000
R RMSE (dBZ)	4.85	4.76	4.59	4.57	4.54	4.48	4.49	4.88
R Cor	0.971	0.971	0.974	0.974	0.974	0.974	0.975	0.969
v_r RMSE (m s^{-1})	1.52	1.52	1.55	1.54	1.55	1.54	1.55	1.62
v_r Cor	0.969	0.969	0.968	0.968	0.968	0.968	0.968	0.965

FIG. 7. Spatially variable U, V fields obtained from the $\beta = 400$ dBZ^2 experiment with KOKC reflectivity data from the 8 May 2003 test case.
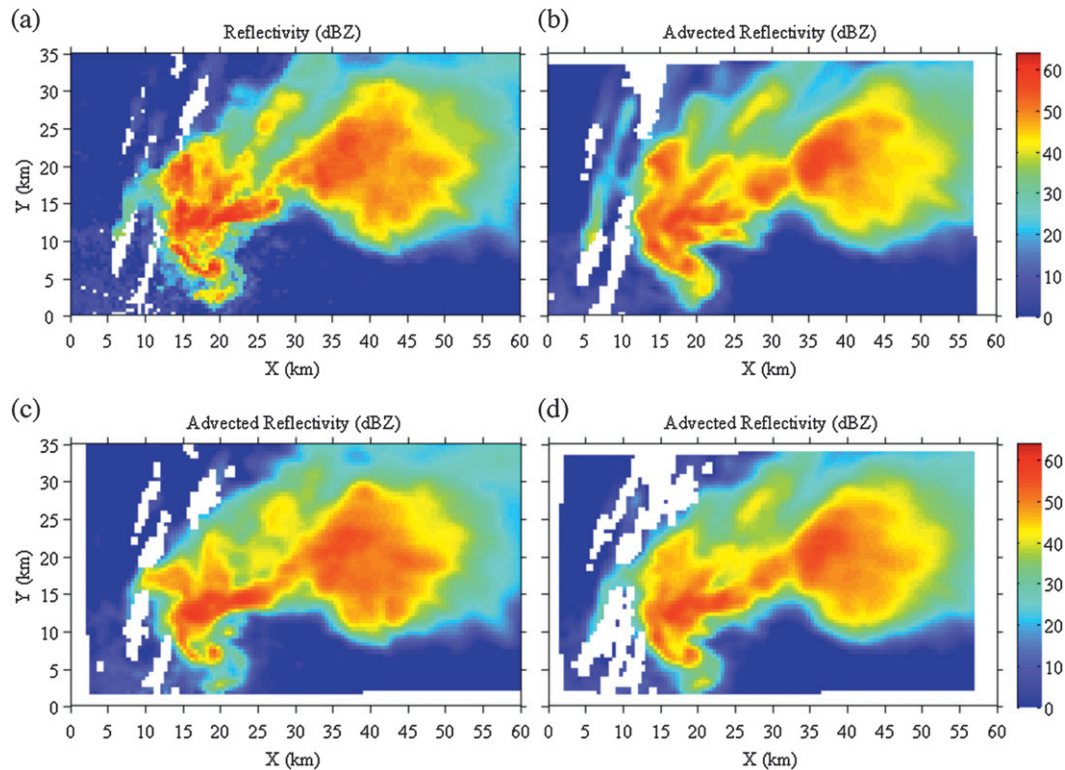
FIG. 8. Reflectivity analyses on the 0.6° elevation angle of the KOKC radar for the 8 May 2003 test case. (a) KOKC reflectivity field at 2225:16 UTC. Reflectivity fields advection-corrected to 2225:16 UTC using (b) forward-only trajectory analysis and data from 2227:17 UTC, (c) backward-only trajectory analysis and data from 2222:55 UTC, and (d) both forward and backward trajectory analysis and data from both 2222:55 and 2227:17 UTC. White areas indicate missing values.

The advection-corrected reflectivity from the $\beta = 400$ dBZ^2 experiment valid at 2225:16 UTC and the corresponding PPI analysis are presented in Figs. 8d and 8a, respectively. The corresponding results from a forward-only trajectory analysis and a backward-only trajectory analysis are shown in Figs. 8b and 8c, respectively. One can see that the advection-corrected reflectivity fields in all three experiments are smoother than the reflectivity fields at the verification PPI time (Fig. 8a) and the input PPI times (Fig. 3). This is due to application of the nine-point smoother, the interpolation of data to the trajectories, and, in the case of the combined forward and backward trajectory analysis (Fig. 8d), the blending of data from two input PPI times. This latter analysis is the smoothest of the three analyses—and the analysis with the smallest errors. Since the backward-only trajectory analysis depicted in Fig. 8c is, by design, very similar to the input reflectivity at the first input time (top left panel of Fig. 3), it is unable to make provision for the "filling in" of the hook echo and the new convective development on the northwestern part of the storm evident at the second input time (top right panel of Fig. 3). Similarly, the forward-only trajectory analysis depicted in Fig. 8b was

not informed of the distinct narrow spiral-like shape of the hook echo at the first input time. In contrast, the combined forward and backward trajectory analysis "splits the difference" between features appearing at the two input times, and yields the best results. An experiment in which the latter analysis was rerun with the nine-point smoother turned off (not shown) yielded a reflectivity field very similar to that obtained with the smoother but with ~2% degradation of the RMSE.

Additional experiments were run to explore the possibility that the analyzed reflectivity field was sensitive to the first guesses for U and V (i.e., due to the potential for solution nonuniqueness identified in Part I). Experiments with β ranging from 25 to 1000 dBZ^2 were rerun with first guesses for U and V set to zero. Such advection fields are even weaker than those used to initialize the original experiments. The results were nearly identical to those obtained previously (differed by less than 0.5% from the values in Table 1), with the exception of experiment B25 where the RMSE had risen to 5.35 dBZ (although, as in the original experiment, the procedure had not converged in B25). Experiments were then rerun with much larger first guesses for U and V, namely

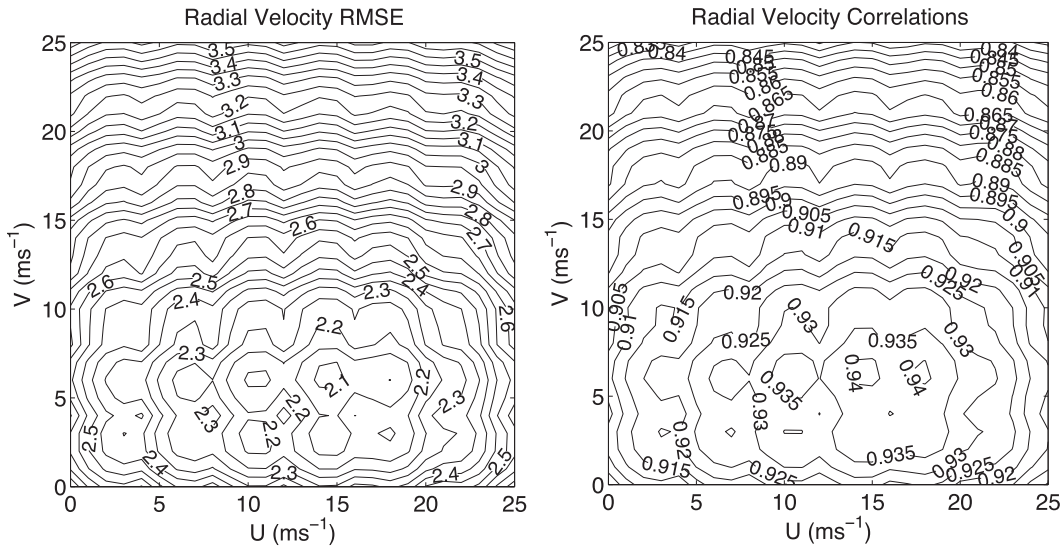FIG. 9. Contour plots of radial velocity (left) RMSE and (right) Cor for 8 May 2003 KOKC advection-correction experiments with imposed constant U, V components and forward-only trajectory analyses. Results are valid at 2225:16 UTC. Contour interval for radial velocity RMSE is 0.05 m s^{-1}. Contour interval for radial velocity Cor is 0.005.

$U = 15$ m s^{-1} and $V = 25$ m s^{-1}. The results in this case differed from those in Table 1 by less than 0.5% for all values of β.

Next, we consider an ad hoc advection-correction procedure for the radial velocity field based on integrating (1.3) from Part I along the trajectories obtained from the reflectivity-based method and imposing the radial velocity data on both end points of those trajectories (i.e., at 2222:55 and 2227:17 UTC). The interpolation formula obtained from (1.3) is

$$v_r(t) = \frac{1}{r(t)} \left\{ r(t_i)v_r(t_i) + \frac{(t - t_i)}{T} \right.$$

$$\left. \times \left[r(t_i + T)v_r(t_i + T) - r(t_i)v_r(t_i) \right] \right\}. \quad (3.2)$$

This advection correction can be easily implemented through minor modifications of the numerical subroutines used in the reflectivity-based procedure. However, since (1.3) is not used in the calculation of the trajectories (presumably that would be the more appropriate constraint
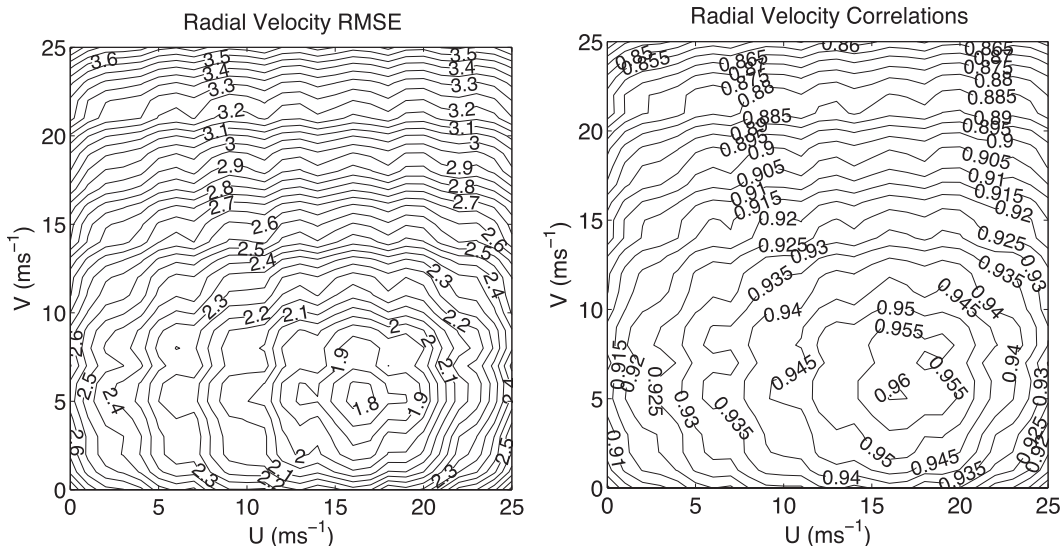

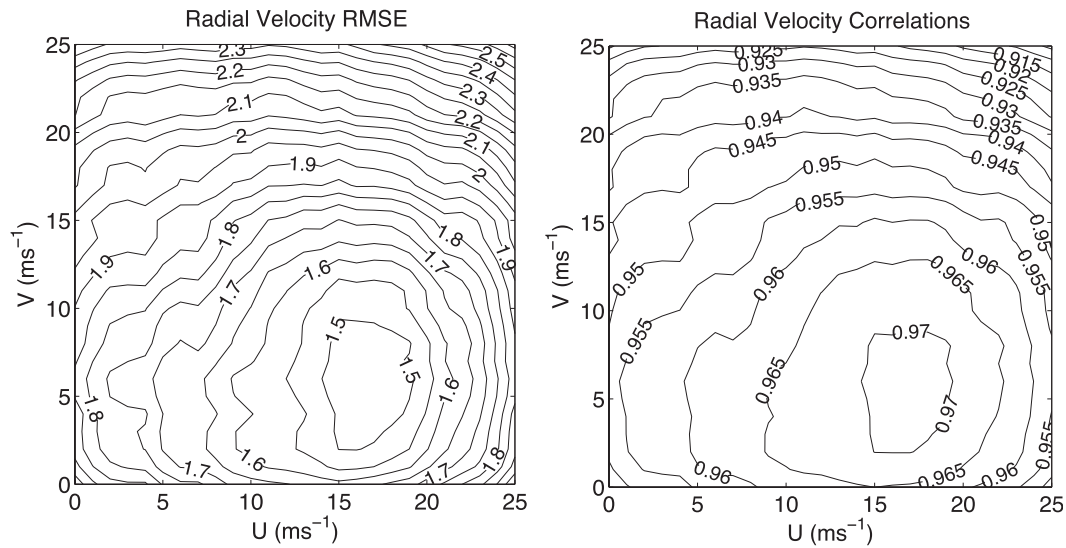FIG. 10. As in Fig. 9, but for backward-only trajectory analyses.

FIG. 11. As in Fig. 9, but for combined forward and backward trajectory analyses.

in this case), it is not clear how useful this ad hoc approach will be. Additionally, since constancy of U and V is invoked in the derivation of (1.3) (Gal-Chen 1982), (3.2) cannot be strictly true for the case of spatially variable U and V, although as long as U and V are smoothly varying, this should be a relatively small source of error. The statistics for experiments with the same range of β considered above are presented in Table 1.
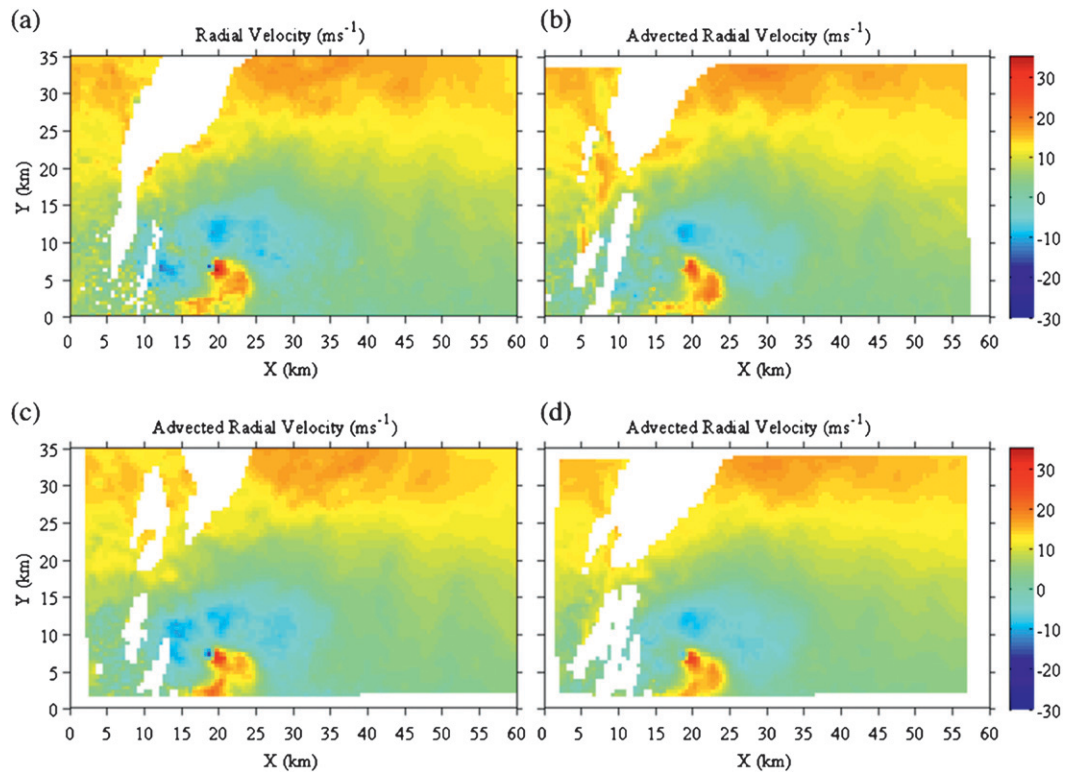

FIG. 12. Radial velocity analyses on the 0.6° elevation angle of the KOKC radar for the 8 May 2003 test case. (a) KOKC radial velocity field at 2225:16 UTC. Radial velocity fields advection-corrected to 2225:16 UTC using (b) forward-only trajectory analysis and data from 2227:17 UTC, (c) backward-only trajectory analysis and data from 2222:55 UTC, and (d) both forward and backward trajectory analysis and data from both 2222:55 and 2227:17 UTC. White areas indicate missing values.

These results can be compared with the results from constant U, V experiments conducted with forward-only trajectory analyses (Fig. 9), backward-only trajectory analyses (Fig. 10), and combined forward and backward trajectory analyses (Fig. 11). One sees that the spatially variable procedure yields results that are better than those obtained from any of the constant U, V forward- and backward-only trajectory analyses but very similar to (actually very slightly worse than) the best of the constant U, V combined forward and backward trajectory analyses. Thus, while use of spatially variable reflectivity-based advection fields yielded generally good results with the advection correction of radial velocity data (RMSE $\simeq 1.5$ m s^{-1}), the spatially variable nature of the advection fields did not add value. Presumably, further improvements in the advection correction of the radial velocity might be attained through use of a purely radial velocity–based analysis procedure. The radial velocity fields produced by the spatially variable procedure run in forward-only, backward-only, and combined forward and backward trajectory analysis modes are depicted in Fig. 12. Compared to the differences between the analyzed reflectivity fields evident in Fig. 8, the differences between the analyzed radial velocity fields in Fig. 12 are relatively subtle. A notable exception is apparent in the vicinity of the tornado ($x \simeq 19$ km; $y \simeq 7$ km), where the backward-only trajectory analysis (Fig. 12c) has the most distinct velocity couplet. This is likely due to the fact that the tornado was actually weakening during the analysis time window, and the backward-only analysis only uses data from the first input time.

Finally, we consider the question of vertical continuity of the U, V fields. Since there is no explicit analysis constraint linking the U, V fields in the vertical, one may ask whether having "well-behaved" input data (data that do not exhibit sharp variations in the vertical) is sufficient to obtain correspondingly well-behaved U, V fields. Since operational TDWR radars sample the atmosphere with relatively coarse resolution in the vertical (elevation angle spacing roughly 3 times that of operational WSR-88D radars), we conducted our vertical continuity tests with data from the KTLX WSR-88D radar. Tests were performed using KTLX reflectivity CAPPIs constructed on the 600-, 1100-, 1600-, and 2100-m (ASL) elevations over the same analysis domain (same size, location, and spatial resolution) and close to the same time period as in the KOKC experiments. The volume scans used in the production of each set of the input CAPPIs began at 2220:54 and 2226:10 UTC (volume scan time for KTLX was ~1 min longer than for KOKC). An example of one of the input CAPPIs is given in Fig. 13. The sequence of U, V fields obtained from the combined forward and backward trajectory analysis with $\beta = 400$ dBZ^2 is shown in Fig. 14.
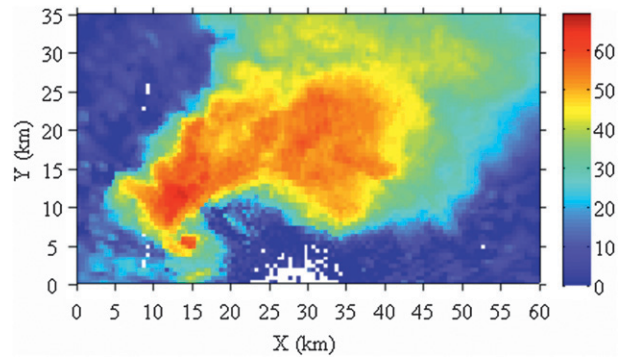

FIG. 13. KTLX reflectivity CAPPI at 600 m (ASL) at 2226:10 UTC 8 May 2003, a time intermediate between the two reflectivity PPI input times in the KOKC experiments (cf. Fig. 3) and ~1 min after the KOKC reflectivity PPI verification time (cf. Fig. 8). Analysis domain is as in Figs. 3 and 8 but is valid at a constant height rather than at a constant elevation angle. The color bar has been slightly altered from that in Figs. 3 and 8 to display the slightly larger peak reflectivity values observed by the KTLX radar. White areas indicate missing values.

One sees immediately that both U and V fields vary only gradually with height. It is also apparent that although the KTLX U, V fields are in qualitatively good agreement with the corresponding KOKC fields, there are some notable differences. In particular, the KTLX U field is up to ~5 m s^{-1} weaker than the KOKC U field in parts of the northern and eastern regions of the domain, while the KTLX V field is up to ~5 m s^{-1} stronger than the KOKC V field in part of the north central region. We speculate that the attenuation of KOKC reflectivity data played a role in some of the discrepancies.

4. Summary and future work

The focus of this two-part study was the development and evaluation of an advection-correction/analysis procedure for radar reflectivity in which the pattern-advection components vary spatially. Part I was concerned with the formulation of the procedure and drawing attention to the possibility that the present method as well as related methods of analysis (e.g., VET) were potentially subject to temporal aliasing (solution nonuniqueness). In Part II, tests of the procedure using analytical reflectivity blobs in a solid-body vortex and using 8 May 2003 TDWR and WSR-88D reflectivity data from a supercell thunderstorm confirmed the utility of the method. In the TDWR tests, the new procedure yielded analyzed reflectivity fields with lower RMSEs and higher correlation coefficients than reflectivity fields that were advection-corrected with any constant advection speed. The qualitatively reasonable advection fields obtained with the new procedure and relative insensitivity to the first guesses of the advection components indicated that
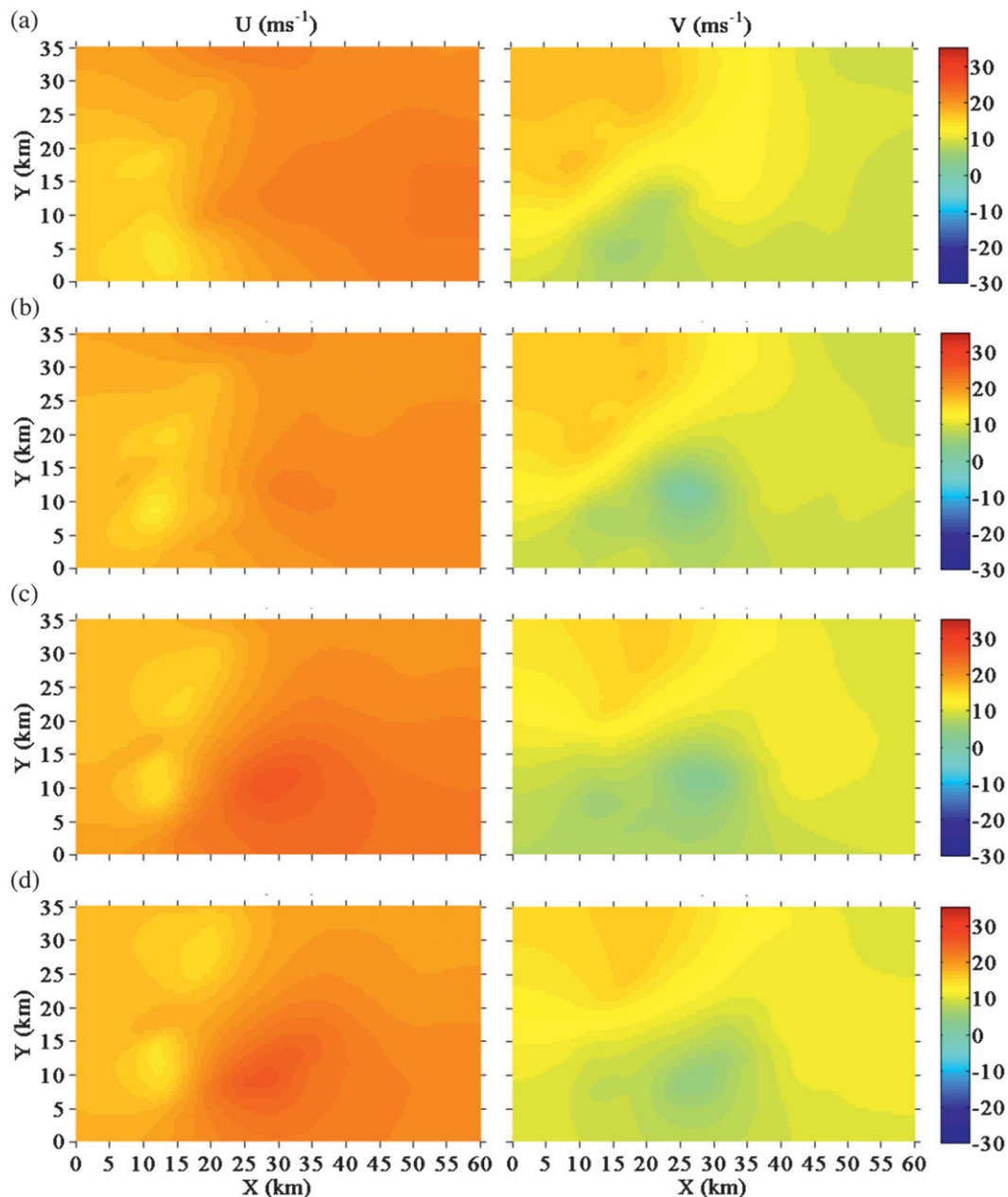
FIG. 14. Spatially variable (left) U and (right) V fields obtained from $\beta = 400 \text{ dB}Z^2$ analyses using KTLX radar reflectivity data from the 8 May 2003 test case. Results are shown for the (a) 600-, (b) 1100-, (c) 1600-, and (d) 2100-m (ASL) elevations.

useful information about the differential motions of reflectivity features was being extracted, and suggested that problems stemming from the potential for solution nonuniqueness did not occur. However, the reader is cautioned that the potential for solution nonuniqueness does exist in this procedure and the related VET method (see Part I). Indeed, Laroche and Zawadzki (1995) and Germann and Zawadzki (2002) have noted multiple minima in the VET cost functions in some of their tests.

Germann and Zawadzki (2002) suggest that, in practice, an accurate analysis can be obtained if one uses a reasonably accurate first guess.

A procedure to advection correct radial velocity data using the same advection fields obtained from the reflectivity-based procedure was also tested with 8 May 2003 TDWR data. Although the results were generally good, the RMSEs were not lower than those obtained in the experiment with the best constant U, V parameters.

We speculate that better results might be obtained using spatially variable U, V fields derived from a purely radial-velocity-based analysis procedure. This will be the subject of a future investigation.

REFERENCES

Aksoy, A., D. C. Dowell, and C. Snyder, 2009: A multicase comparative assessment of the ensemble Kalman filter for assimilation of radar observations. Part I: Storm-scale analyses. *Mon. Wea. Rev.,* **137,** 1805–1824.

Crum, T. D., and R. L. Alberty, 1993: The WSR-88D and the WSR-88D Operational Support Facility. *Bull. Amer. Meteor. Soc.,* **74,** 1669–1687.

Donner, K. M., 2007: High-resolution dual-Doppler analysis of two tornadic thunderstorms using a new formulation of advection-correction. M.S. thesis, School of Meteorology, University of Oklahoma, 176 pp.

Dowell, D. C., and L. J. Wicker, 2009: Additive noise for storm-scale ensemble data assimilation. *J. Atmos. Oceanic Technol.,* **26,** 911–927.

Gal-Chen, T., 1982: Errors in fixed and moving frame of references: Applications for conventional and Doppler radar analysis. *J. Atmos. Sci.,* **39,** 2279–2300.

Germann, U., and I. Zawadzki, 2002: Scale-dependence of the predictability of precipitation from continental radar images. Part I: Description of the methodology. *Mon. Wea. Rev.,* **130,** 2859–2873.

Haltiner, G. J., and R. T. Williams, 1980: *Numerical Prediction and Dynamic Meteorology.* John Wiley and Sons, 477 pp.

Hu, M., and M. Xue, 2007: Impact of configurations of rapid intermittent assimilation of WSR-88D radar data for the 8 May 2003 Oklahoma City tornadic thunderstorm case. *Mon. Wea. Rev.,* **135,** 507–525.

Klazura, G. E., and D. A. Imy, 1993: A description of the initial set of analysis products available from the NEXRAD WSR-88D system. *Bull. Amer. Meteor. Soc.,* **74,** 1293–1311.

Kumjian, M. R., and A. V. Ryzhkov, 2008: Polarimetric signatures in supercell thunderstorms. *J. Appl. Meteor. Climatol.,* **47,** 1940–1961.

——, and ——, 2009: Storm-relative helicity revealed from polarimetric radar measurements. *J. Atmos. Sci.,* **66,** 667–685.

Laroche, S., and I. Zawadzki, 1995: Retrievals of horizontal winds from single-Doppler clear-air data by methods of cross correlation and variational analysis. *J. Atmos. Oceanic Technol.,* **12,** 721–738.

Liu, S., M. Xue, and Q. Xu, 2007: Using wavelet analysis to detect tornadoes from Doppler radar radial-velocity observations. *J. Atmos. Oceanic Technol.,* **24,** 344–359.

Michelson, M., W. W. Shrader, and J. G. Wieler, 1990: Terminal Doppler weather radar. *Microwave J.,* **33,** 139–148.

NOAA/NWS, 2005: TDWR interface control and specifications documentation for the NWS supplemental product generator, version 4.3, 42 pp. [Available online at http://wdtb.noaa.gov/buildTraining/TDWR/TDWR_SPG_ICD_v43.pdf.]

Oye, D., and M. Case, 1995: REORDER: A program for gridding radar data—Installation and use manual for the UNIX version. Atmospheric Technology Division, National Center for Atmospheric Research, 20 pp. [Available from Atmospheric Technology Division, NCAR, P.O. Box 3000, Boulder, CO 80307.]

Oye, R., C. Mueller, and S. Smith, 1995: Software for radar translation, visualization, editing, and interpolation. Preprints, *27th Conf. on Radar Meteorology,* Vail, CO, Amer. Meteor. Soc., 359–361.

Potvin, C. K., A. Shapiro, T. Y. Yu, J. Gao, and M. Xue, 2009: Using a low-order model to detect and characterize tornadoes in multiple-Doppler radar data. *Mon. Wea. Rev.,* **137,** 1230–1249.

Romine, G. S., D. W. Burgess, and R. B. Wilhelmson, 2008: A dual-polarization-radar-based assessment of the 8 May 2003 Oklahoma City area tornadic supercell. *Mon. Wea. Rev.,* **136,** 2849–2870.

Ryzhkov, A. V., T. J. Schuur, D. W. Burgess, and D. S. Zrnic, 2005: Polarimetric tornado detection. *J. Appl. Meteor.,* **44,** 557–570.

Shapiro, A., K. M. Willingham, and C. K. Potvin, 2010: Spatially variable advection correction of radar data. Part I: Theoretical considerations. *J. Atmos. Sci.,* **67,** 3445–3456.

Shun, C. M., S. Y. Lau, and O. S. M. Lee, 2003: Terminal Doppler weather radar observation of atmospheric flow over complex terrain during tropical cyclone passages. *J. Appl. Meteor.,* **42,** 1697–1710.

Vasiloff, S. V., 2001: Improving tornado warnings with the Federal Aviation Administration's terminal Doppler weather radar. *Bull. Amer. Meteor. Soc.,* **82,** 861–874.

Wang, Y., T. Y. Yu, M. Yeary, A. Shapiro, S. Nemati, M. Foster, D. L. Andra, and M. Jain, 2008: Tornado detection using a neuro-fuzzy system to integrate shear and spectral signatures. *J. Atmos. Oceanic Technol.,* **25,** 1136–1148.